DTU Library

An offshore reservoir monitoring system based on fiber optic sensing of seabed strains

Levenberg, Eyal; Orozova-Bekkevold, Ivanka; Nielsen, Kristian

[Link back to DTU Orbit](#)

An offshore reservoir monitoring system based on fiber optic sensing of seabed strains

Eyal Levenberg and Ivanka Orozova-Bekkevold (DTU Civil Engineering), and Kristian Nielsen (DTU Photonics Engineering)

Abstract

One of the problems affecting mature fields in the North Sea is seabed subsidence due to reservoir depletion. Seabed subsidence can directly affect integrity of production facilities. Severe subsidence, as in the case of the Ekofisk field, can lead to platform sinking below the sea level and, subsequently, to very high repair costs or possibly to a complete platform replacement. Subsidence is an issue also in the Tyra field, and it will become a problem in other fields as depletion is taking-off. Fluid injection is a widely used method to boost production and/or maintain reservoir pressure in order to mitigate compaction and subsidence. Both reservoir depletion and fluid injection operations induce seabed deformations. The deformation pattern potentially holds useful information about production efficiency and reservoir management, which could be captured by careful and continuous monitoring of seabed strains. Current technologies for monitoring offshore seabed deformations only provide point or line readings. The idea that this sprint project explores is achieving nearly full-field and continuous monitoring of seabed surface deformations by means of distributed fiber optic sensors. The objective of the study was to theoretically assess whether current fiber optic sensing technology is sensitive enough to detect production-induced seabed strains originating at a 2000 m deep reservoir.

1. Technology vision

The Danish gas fields in the North Sea are produced by natural depletion with gas/fluid expulsion and related compaction as drivers [1]. Often, reservoir compaction is translated into seabed subsidence, which has a direct adverse effect on production facilities. Such subsidence, as in the case of the Tyra gas field, is of the order of 200 mm per year. To a lesser extent, seabed subsidence is also observed in oil fields such as Dan. Initially, the Dan field was produced by natural depletion - with water injection initiated only after 8 years of production. Despite water injection, seabed subsidence has continued, indicating that the compaction drive remained active. Modern developments, such as the Halfdan Field, have parallel injection and producer wells resulting in near-zero seabed subsidence. Nevertheless, pressure differences between injector and producer wells may

have caused minor deformations of the seabed - leading to minor positive and negative vertical displacements at the different Halfdan platforms. It is reasonable to assume that loss of pressure support caused by short circuits between injector and production wells might have been the reason for the observed deformations. To the best of our knowledge, these displacement ripples have yet to be thoroughly investigated.

The technology vision proposed in this project is to develop a reservoir monitoring system based on reading seabed deformations by the means of distributed fiber optic strain sensing technology, with fiber optic cables coupled to the seabed. The idea is conceptually shown in Figure 1. The sketch on the left is an overhead view of a production field (e.g., Tyra), showing a single-cable distributed fiber optic sensor system deployed around a platform. The shown meshing is geared towards reading radial and tangential strains w.r.t. a cylindrical coordinate system positioned at the bottom of the platform. Redundancy is assured by loops periodically returning to the platform. Thus, a damaged loop can be skipped by splicing operations taking place on the platform - without expensive underwater gear. In practice, the deployment pattern must be tailored to the production setup with fiber orientations corresponding to the anticipated principal strain directions. The center (middle) image in Figure 1 shows a Fugro seabed trencher - a semi-robotic device that can potentially deploy a fiber optic cable according to a desired pattern [2]. This device buries a cable at a depth of about two meters below the seabed thus ensuring mechanical coupling with the surrounding soil medium. Such burial depth also provides protection against fishing trawls and isolation from storm effects. The estimated cost of such deployment is about 2.5 million DKK per kilometer. The sketch on the right hand side of Figure 1 illustrates how fiber optic cables can be brought to the platform deck through a J-tube in order to be connected to a fiber optic interrogator which consists of a delicate laser source and receiver optics [3].
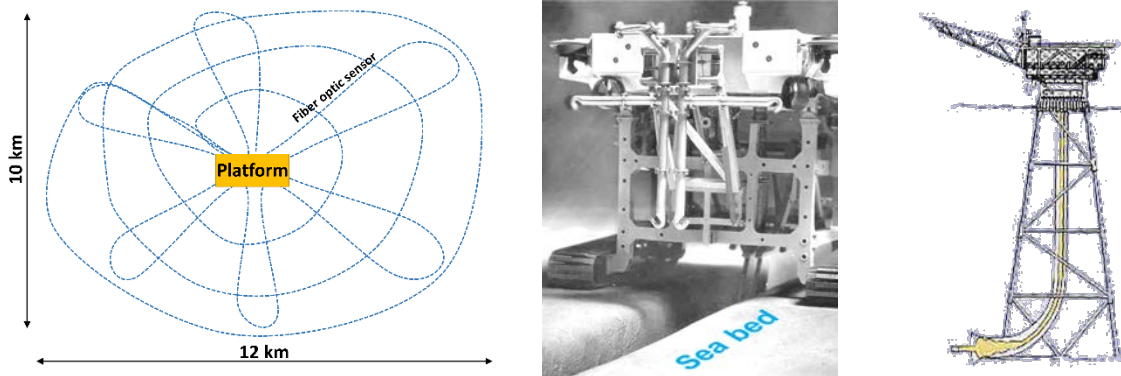
Figure 1: Possible deployment pattern for a fiber optic sensor around an offshore platform (left), Fugro seabed trencher for sensor embedment (center), and J-tube for bringing fiber optic cables onto the platform (right).

Fiber optic strain sensing is an established technology, commonly employed for monitoring Civil Engineering facilities [4]. Fiber optic sensors have also been employed in the oil and gas industry, as point strain sensors [5] or along pipes [6]. A recent survey of fiber optic sensing applications within the oil and gas industry can be found in [7]. Ideally, the monitoring system should be deployed and activated before the start of production. For already producing fields (such as in the North Sea), a fiber optic monitoring system deployed

after the start of production will sense only events/changes subsequent to installation. In either situation, the proposed system offers several potential benefits: (i) help in monitoring and prediction of reservoir compaction and related subsidence, (ii) provide indication on possible location of short circuits between injection and production wells, (iii) monitor and/or predict the changes in the gap between the deck of the platforms and the sea surface, (iv) provide additional input to 4D seismic surveys, (v) monitor potential smart water that can increase the compaction drive, (vi) monitor induced seismicity due to production activities, and (vii) monitor post-production deformations to accommodate any future environmental inquiries by the authorities. These benefits lead to better decisions on production, re-development, and end-of-field life strategies. By very nature, the system has an advantage over pipeline surveys which provide only information along a line, with readings that are susceptible to pipe corrosion, pipe failure, submarine storms, etc. Furthermore, when a reliable technology arises, capable of reading fiber strains at a very fast rate of the order of 10 kHz, the deployed cables can be utilized as geophones. In this case, considerable price reduction in acquiring 4D seismic data is anticipated [**8**].

Fiber optic strain sensing is based on the so-called Brillouin scattering effect wherein the light intensity in the fiber locally modifies the density of the solid, resulting in scattering and frequency shift [**9**]. Optical detection systems currently available on the market for distributed strain sensing operate with standard telecommunications optical fibers. One example of a relevant interrogator is OZOptics' Foresight™ series of fiber optic Distributed Strain and Temperature Sensors (DSTS). This device uses stimulated Brillouin scattering to independently measure changes in both strain and temperature along the length of an optical fiber. Temperature readings are needed to annul temperature-related strains. The maximum sensing length for this system is 100 km (fiber length can be 160 km) with a resolution of 0.1 microstrains and accuracy of ±2 microstrains. If desired, the spatial resolution can be as short as 5 cm. The device is of the size a desktop computer with a cost of about 1 million DKK.

2. Validation of technology

The main objective of the current work was to carry out an in silico feasibility study of whether current fiber optic sensing technology has the measurement ability in terms of resolution and accuracy to detect production-induced seabed strains. Such assessment is a first and necessary step before any further development because the associated strains are expected to be very small.

2.1. Analytic Modeling

An existing analytic theory for computing mechanical responses due to deep deformations was employed as a basic modeling tool [**10**]. The theory considers (see Figure 2) a weightless, isotropic, homogeneous, and linear elastic layer with thickness H and material properties E (Young's modulus) and ν (Poisson's ratio), which is infinite laterally. Herein, this layer represents the overburden, i.e., the entire strata overlaying a reservoir. Initially, the medium is assumed to be undeformed and stress-free, with both top and bottom boundaries completely flat (dash-dot lines), i.e., any existing stresses due to self-weight are taken as initial conditions and

therefore annulled. Next, an axisymmetric blister-like displacement field is imposed at the bottom of the layer, forcing the lower boundary to deform vertically, without inducing shear stresses at the interface (solid line).
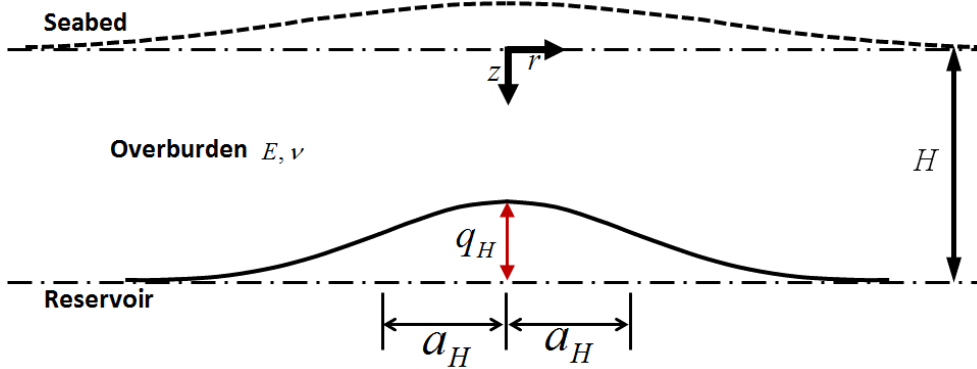

Figure 2: Illustration of basic model definitions.

The modeling allows for calculating all mechanical responses (i.e., stresses, strains, and displacements) inside the layer as well as at the top - corresponding to the seabed level. To facilitate the formulation, a cylindrical coordinate system is included in the Figure, with its origin placed at the top of the undeformed layer, the depth z-axis drawn into the medium, and the radial r-axis ($r \geq 0$) parallel to the top boundary. The imposed displacement field at bottom is denoted by u_z^H, mathematically expressed as an axisymmetric Gaussian:

$$u_z^H(r) = q_H e^{-(r/a_H)^2/2} \tag{1}$$

where r is the radial coordinate, q_H is the peak displacement occurring at $r = 0$, and a_H represents the location where the curvature of $u_z^H(r)$ changes sign (i.e., inflection point). Both q_H and a_H have units of length; a_H must be positive, while q_H can be either positive or negative to indicate downward or upward deformation (respectively). The particular form of Equation 1 was chosen because it can serve as a radial basis function for representing any other deformation shapes - not necessarily axisymmetric [11]. This modeling flexibility is needed when simulating, e.g., the effects of a producer-injector array.

The mechanical responses at the top of the layer (where $z = 0$) are calculated from the following equations:

$$\sigma_r^0 = -E \int_{m=0}^{\infty} \left\{ \left[mJ_0(m\rho) - \frac{J_1(m\rho)}{\rho} \right] \left\{ \begin{matrix} [A+C]e^{-m} \\ +B-D \end{matrix} \right\} + 2\nu m J_0(m\rho) \left[Ce^{-m} - D \right] \right\} dm \tag{2}$$

$$\sigma_\theta^0 = -E \int_{m=0}^{\infty} \left\{ \frac{J_1(m\rho)}{\rho} \left[Ae^{-m} + Ce^{-m} + B - D \right] + 2\nu m J_0(m\rho) \left[Ce^{-m} - D \right] \right\} dm \tag{3}$$

4

$$u_z^0 = -H(1+v) \int\limits_{m=0}^{\infty} \left\{ J_0(m\rho) \left[Ae^{-m} - C(2-4v)e^{-m} - B - D(2-4v) \right] \right\} dm \tag{4}$$

$$u_r^0 = H(1+v) \int\limits_{m=0}^{\infty} \left\{ J_1(m\rho) \left[Ae^{-m} + Ce^{-m} + B - D \right] \right\} dm \tag{5}$$

where σ_r^0, σ_θ^0, u_z^0, and u_r^0 denote (respectively) radial stress, tangential stress, vertical displacement, and radial displacement; m is a unitless integration parameter. The superscript zero indicates that these responses are calculated at $z=0$. Moreover, $\rho = \rho(r) = r/H$ is a normalized (dimensionless) radial coordinate, $J_0(\cdot)$ and $J_1(\cdot)$ are Bessel functions of the first kind of order zero and one (respectively), and A, B, C, and D are each a dimensionless function of m. The latter are obtained from enforcing the problem boundary conditions; they are explicitly listed in [12]. Seabed strains, expected to be read by the fiber optic sensors, are derived from the stresses in the usual way:

$$\varepsilon_r^0 = \frac{\sigma_r^0 - v\sigma_\theta^0}{E} \quad \text{and} \quad \varepsilon_\theta^0 = \frac{\sigma_\theta^0 - v\sigma_r^0}{E} \tag{6}$$

where ε_r^0 and ε_θ^0 denote the strain in the radial direction and tangential direction (respectively). Note that these strains are not affected by the overburden modulus because it cancels-out when inserting the stress expressions from Equations 2 and 3.

Two scenarios are considered hereafter. The first deals with simulating the conditions of depletion-induced subsidence, for example in the case of gas production. The second deals with monitoring a stimulated field consisting of an array of producers and injectors. For both cases it is assumed that the strain monitoring system is deployed and activated at some point in time after the start of production operations, and therefore detects only subsequent events.

2.2. Simulation of depletion-induced subsidence

The model is first utilized for simulating depletion-induced subsidence over a large area. The overall compaction at top reservoir (equivalent to the bottom of the overburden) is idealized as being axisymmetric according to Equation 1. The assumed model parameters are: (i) overburden thickness $H = 2000\,\text{m}$, (ii) Poisson's ratio of medium $v = 0.26$, (iii) width of Gaussian representing displacement pattern at the reservoir top $a_H = 1000\,\text{m}$, and (iv) peak reservoir compaction $q_H = 300\,\text{mm}$ representing an annually expected value.

Model calculation results are shown in Figures 3 and 4. Figure 3 presents the vertical displacement fields at top reservoir (bottom charts depicting u_z^H) and at the seabed level (top charts depicting u_z^0). It can be seen that the induced displacement is attenuated at the seabed. The peak vertical displacement drops from 300 mm (assumed at top reservoir) to about 180 mm at seabed (top of overburden). Also, the deformation pattern (i.e., subsidence bowl) is somewhat wider at the surface. Figure 4 presents the corresponding seabed strains in the

radial (bottom charts) and tangential (top charts) directions. It can be seen that radial strains (ε_r^0) change sign from positive (compression) to negative (tension) while the tangential strains (ε_θ^0) are only compressive. The strain levels in both directions are of the order of 50 microstrains, i.e., within the resolution and accuracy limits of current fiber optic sensing technology – and therefore detectable.
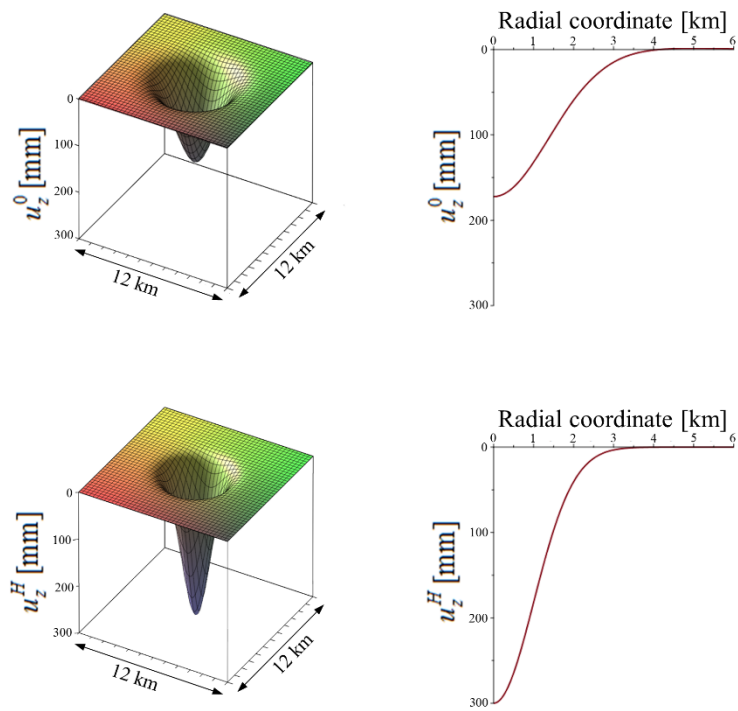

Figure 3: Vertical displacement field in the axisymmetric case; reservoir (bottom charts) and seabed level (top charts).
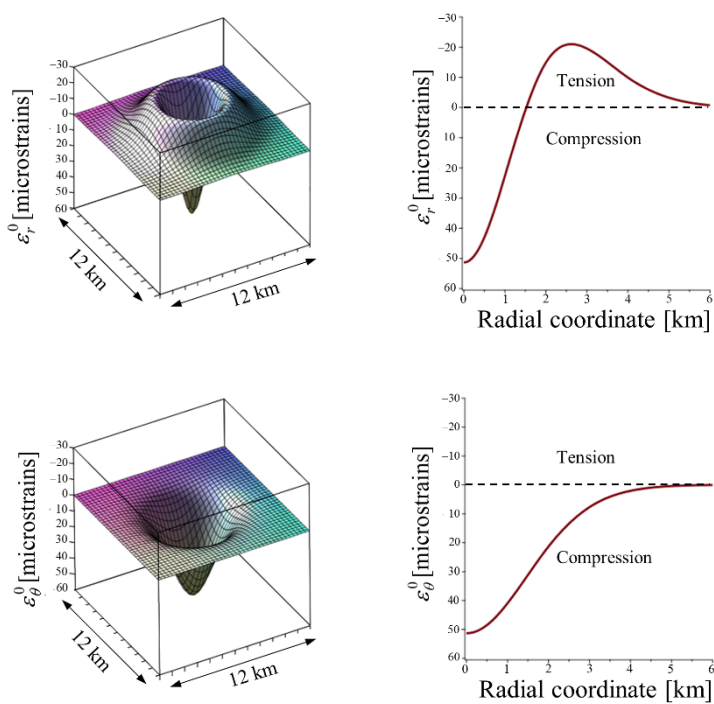
Figure 4: Seabed strain distributions in the axisymmetric case; radial (top charts) and tangential (bottom charts).

2.3. Simulation of injector-producer array

The second considered case simulated a virtual injector-producer array consisting of 3 producers (denoted as $P_1...P_3$) and 4 injectors (denoted as $I_1...I_4$). The array is arranged as shown in Figure 5 (left hand side) with L denoting length and W denoting spacing between injectors and producers. A Cartesian coordinate system is employed in this case, with the y-axis oriented parallel to the wells, the x-axis pointing in the transverse direction, and the z-axis (not shown) pointing downward towards the earth's core. A proposed pattern for fiber optic sensor deployment, matching the geometry of the injector-producer array (and the expected principal strain directions), is shown on the right hand side of Figure 5. As can be seen, the pattern includes several loops, generally oriented in the directions of the x and y axes. As in Figure 1, redundancy and ease of maintenance is enabled by periodically returning the fiber to the platform to enable splicing in case of a damage loop.
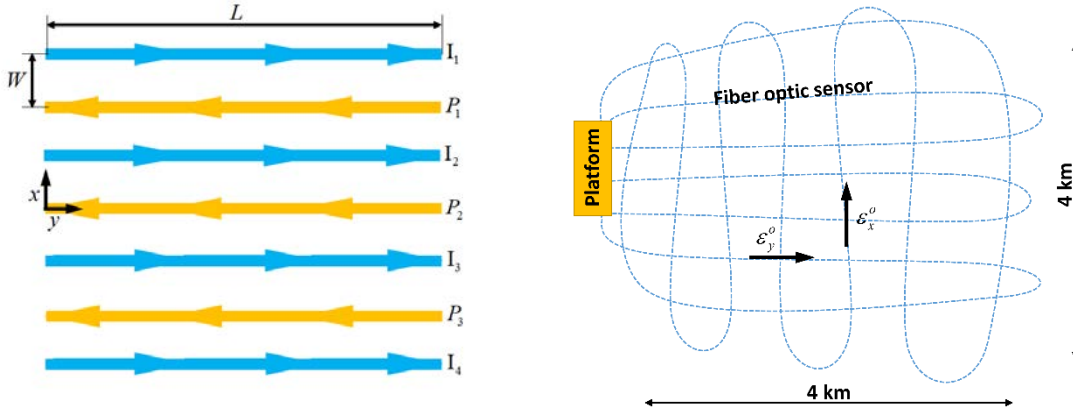

Figure 5: A virtual injector-producer array (left) and a possible fiber deployment pattern (right).

Under operation, the injector-producer array in Figure 5 imposes vertical deformations at the bottom of the overburden (top reservoir) - depression in the vicinity of the producers and heaving in the vicinity of the injectors. Such deformation pattern can be approximated mathematically by the following expression:

$$u_z^{IP} = \frac{A}{2}\cos\left(\frac{\pi x}{W}\right)\left(\begin{array}{l}\left(\begin{array}{l}H(x-0.5W)-H(x+0.5W)\\+H(x-1.5W)-H(x+1.5W)\end{array}\right)H(sL+y-L)\\+\left(\begin{array}{l}H(x+0.5W)-H(x-0.5W)\\+H(x+1.5W)-H(x-1.5W)\\+2H(x-3.5W)-2H(x+3.5W)\end{array}\right)H(y-L)\\-2\left(\begin{array}{l}H(x-3.5W)\\-H(x+3.5W)\end{array}\right)H(y)\end{array}\right) \tag{7}$$

where u_z^{IP} is the vertical displacement magnitude at the reservoir level at an arbitrary location/point identified by coordinates x and y. The parameter A denotes the displacement amplitude induced by either an injector

or a producer, and $H(\square)$ is the Heaviside step function. The parameter s can range between zero and unity; it is introduced to represent a shortcut event between injector wells I_2 and I_3. If this condition occurs, the heave amplitude caused by I_2 and I_3 is reduced by 50% along a length of sL. At the same time, the depression along P_2 becomes limited to a length $L(1-s)$. In other words, when $s=0$ the injector-producer array is fully operational, and when $s>0$ a partially operational situation is simulated. A full shortcut between I_2 and I_3 is simulated when $s=1$.

Assuming that a strain monitoring system is installed at the seabed when the array is fully functional ($s=0$ condition), subsequent strain readings will reflect deformations caused by any shortcut event, i.e., the difference between $u_z^{IP}(s>0)$ and $u_z^{IP}(s=0)$. This situation is illustrated in Figure 6. The top 3 charts provide plots of u_z^{IP} for different s values. The bottom three charts depict the corresponding displacements (at top reservoir) that generate strains at the seabed level. The common parameters for preparing the charts were: $W=200\,\mathrm{m}$, $L=2\,\mathrm{km}$ and $A=1\,\mathrm{m}$. The correctness of the latter value should be a subject of further study given that the real peak displacement magnitude near the injectors and producers it is not known. The vertical axes in the charts in Figure 6 are graphically distorted ($\times50$), so that the deformation pattern can be noticed.

Figure 7 shows the estimated seabed strains corresponding to the three cases in Figure 6 (bottom three charts), i.e., for the three different s values (0.25, 0.50, and 0.75). The top three charts depict seabed strains in along the x-axis direction (ε_x^0) and the bottom three charts depict seabed strains along the y-axis direction (ε_y^0). As it can be seen, the peak-to-peak strain magnitudes are of the order of a few tenths of a microstrain. These strain levels are similar in magnitude to the current resolution limits of fiber optic sensing (about 0.1 microstrains), and about an order of magnitude smaller than the accuracy limits of the technology (about ±2 microstrains).
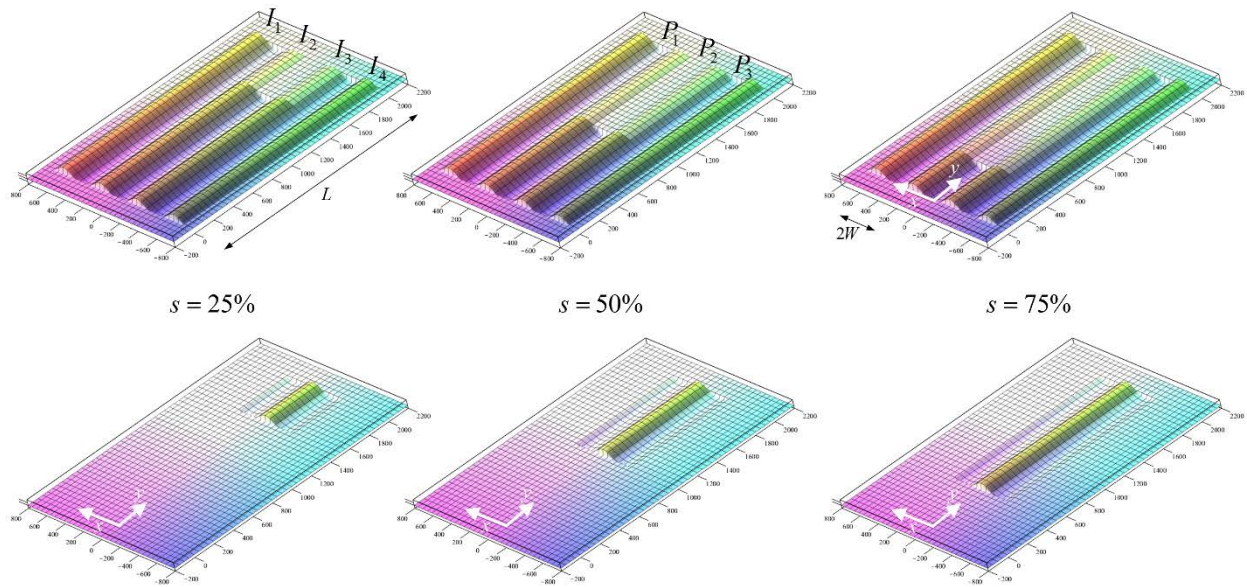

Figure 6: Simulating a partially-operational Injector-Producer array (refer to Figure 5). The top three charts represent the assumed displacement pattern for different shortcut lengths (expressed via the s

parameter) according to Equation 7; the bottom three charts display the corresponding differences in displacements.
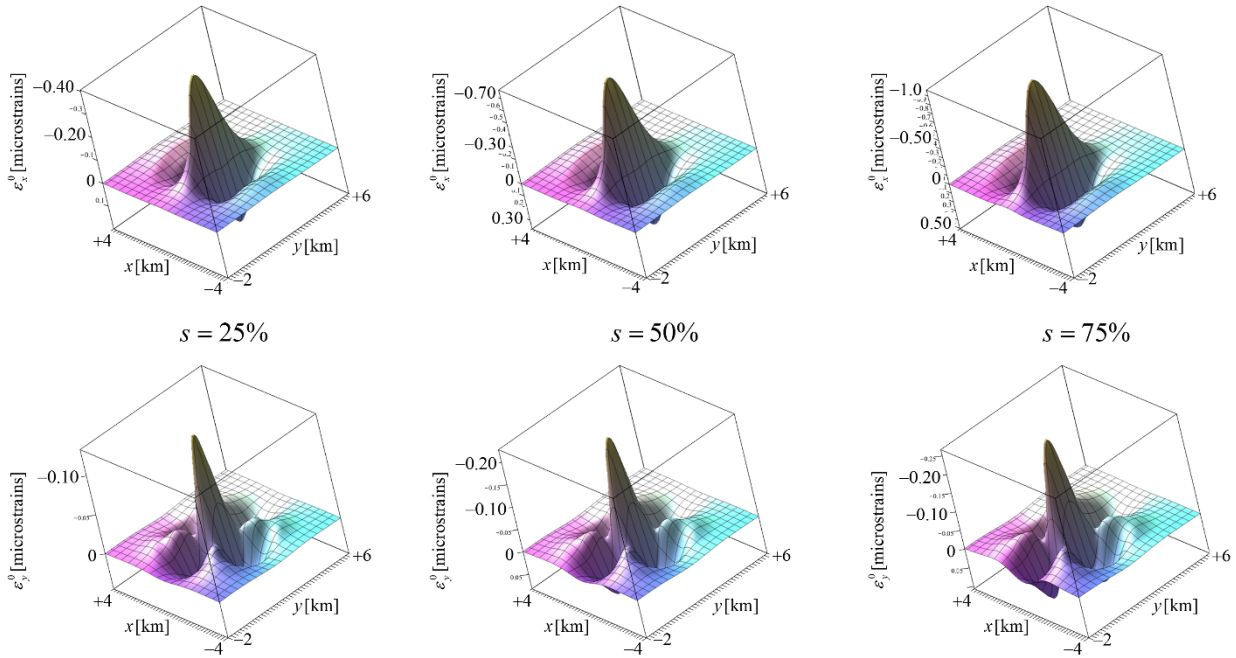

Figure 7: Calculated seabed strains in the x and y directions (see coordinates in Figures 5 and 6) corresponding to three different shortcut cases (refer to bottom charts in Figure 6).

3. Summary and conclusions

This work considered the idea of meshing the seabed near offshore platforms with fiber optic sensors as means of detecting deformations originating at the reservoir level. An analytic model was employed to estimate the magnitude and orientation of expected strains as a first-step feasibility study. Two separate cases were investigated: (i) monitoring the annual compaction of an entire field (see Figure 1), and (ii) monitoring the effects of shortcuts in an injector-producer array (see Figure 5). Based on the calculations, is it concluded that the expected seabed strain levels in the first case are detectable and measurable with current fiber optic sensing technology, while the strain levels in the second case are very small, within the resolution limits of commercially available technology.

3.1. Proposed way forward

The idea proposed in this study appears very promising and practical, and it is therefore suggested to invest further research resources in promoting its realization. The following is a list of recommended actions: (i) improve the modeling by incorporating actual/more detailed production data and compaction/subsidence measurements, (ii) improve the modeling by considering a stratified overburden, (iii) improve the modeling by considering more advanced material behavior e.g., time-dependent properties and permanent deformation properties, (iv) investigate the expected displacements induced by an injector-producer array, (v) construct a scaled-down controlled field experiment where optic fibers are physically deployed, and a buried actuator

mechanically simulates reservoir displacements, (vi) develop an inverse analysis scheme that accepts as input fiber readings, and provides as output information about the reservoir, (vii) investigate distributed fiber optic sensor readings in combination with other instruments such as geophones and tilt-meters, (viii) investigate physical deployment issues, and (ix) perform cost-effectiveness analysis.

References

[1] Danish Energy Agency (2013), "Oil and gas production in Denmark (and subsoil use)," Online report accessed November 20, 2017: https://ens.dk/sites/ens.dk/files/OlieGas/oil_and_gas_in_denmark_2013.pdf.

[2] Fugro Inc., "TSM Q1400 Trenching System," Online link accessed November 20, 2017: youtube.com/watch?time_continue=7&v=cFxlwWPm4f0.

[3] Online image link accessed November 27, 2017: http://pipelineencyclopedia.blogspot.dk/2010/07/j-tube.html.

[4] Barrias, A., Casas, J.R., and Villalba, S. (2016), "A review of distributed optical fiber sensors for civil engineering applications," Sensors, Vol. 16/748, pp. 1–35.

[5] Yanlin, W., Bi Xiangjun, B., Sheng, F., Yingxin, M., and Qianjin, Y. (2011), "Subsidence monitoring of offshore platforms," Procedia Engineering, Vol. 15, pp. 1015–1020.

[6] Inaudi, D. and Glisic, B. (2010), "Long-range pipeline monitoring by distributed fiber optic sensing," Journal of Pressure Vessel Technology, Vol. 132(1), pp. 011701(1)–011701(9).

[7] Daniel, J.S., Maida, J.L., and Skinner, N.G. (2017), "Adapting optical technology to dynamic energy prices: fiber-optic sensing in the contemporary oil field," SPIE Proceedings Vol. 10208: Fiber Optic Sensors and Applications XIV, Anaheim, California, United States.

[8] Maas, S.J. and Buchan, I. (2007), "Fiber optic 4C seabed cable for permanent reservoir monitoring," Proceedings of the International Symposium on Underwater Technology and Workshop on Scientific use of Submarine Cables Related Technologies, Tokyo, Japan, pp. 411–414.

[9] Galindez-Jamioy, C.A. and López-Higuera, J.M. (2012), "Brillouin distributed fiber sensors: an overview and applications," Journal of Sensors, Article ID 204121.

[10] Levenberg, E. (2013), "Analysis of pavement response to subsurface deformations," Computers and Geotechnics, Vol. 50, pp. 79–88.

[11] Goshtasby, A. and O'Neill, W.D. (1993), "Surface fitting to scattered data by a sum of Gaussians," Computer Aided Geometric Design, Vol. 10(2), pp. 143–156.

[12] Levenberg, E. (2015), "Intrinsic roughness mitigation of pavements on expansive soils - an analytic investigation," International Journal of Pavement Research and Technology, Vol. 8(3), pp. 167–171.